Where photons meet phonons

Buters, F.M.

Citation

Buters, F. M. (2017, December 21). *Where photons meet phonons*. *Casimir PhD Series*. Retrieved from https://hdl.handle.net/1887/58471

Author: Buters, F.M.
Title: Where photons meet phonons
Issue Date: 2017-12-21

7

Intermezzo: picking up not-so-good vibrations

7.1 The issue of vibrations

In the previous chapters, optical side-band cooling was successfully used to cool the mechanical motion of a trampoline resonator. For example, in chapter 5 an effective temperature of 4 K is reached. Of course an even lower temperature is possible when more laser power is used. In Fig. 7.1 the mechanical power spectrum of a single trampoline resonator optically cooled to 300 mK is shown. It is clear that only with some imagination a Lorentzian (red line) is present in the data. Because our detection method relies on a clean Lorentzian signal, this clearly poses a problem. This chapter is devoted to finding the origin of the vibrations seen in Fig. 7.1. Two major candidates are discussed: up-conversion of low frequency vibrations and vibrations coming from the sample itself. The low frequency vibrations are investigated using a full numerical simulation, while the sample itself is investigated by measuring resonators with different frequencies and varying the clamping method.

7.2 Low frequency vibrations

7.2.1 Introduction

It might seem strange that low frequency (0-5 kHz) vibrations can have an effect at frequencies above 300 kHz. The optomechanical interaction, however, is parametric in nature, as is shown in chapter 3. Low frequency cavity displacements mix with the motion of the trampoline resonator to create new frequency components at sum and difference frequencies. This becomes quite involved when multiple frequency components are present, as we will show later.

In principle low frequency motion of the cavity length (or laser frequency) should not be an issue, since the laser is locked directly to the cavity resonance. If, however, the feedback is not done properly or the signals to compensate are simply too big, this could cause the vibrations visible in Fig. 7.1. To fully understand the experimen-

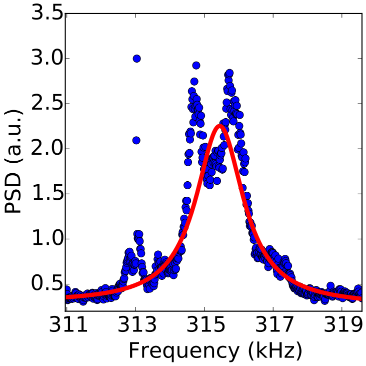

Figure 7.1: Mechanical power spectrum of a single trampoline resonator optically cooled to 300 mK.

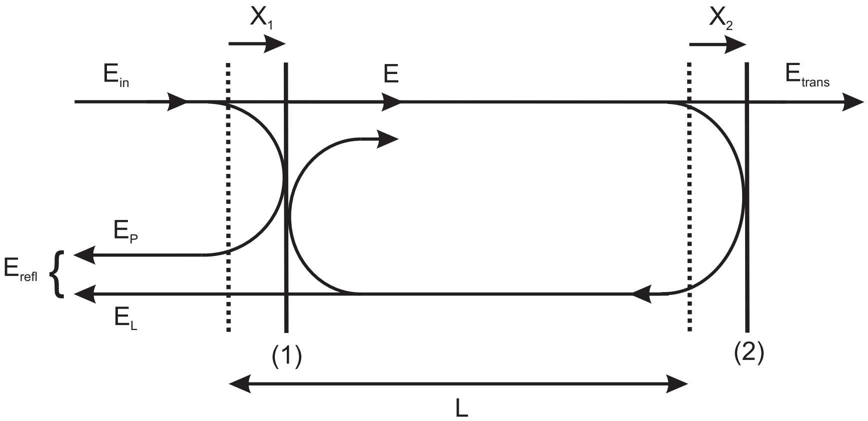

Figure 7.2: The field inside a Fabry-Perot cavity.

tal set-up, a computational platform where the laser detuning or cavity length can be varied together with a read-out of the mirror motion in accordance with experiment is needed. The next sections outline the computational steps required to fully model the experiment.

7.2.2 Theory

Definitions

The field inside a Fabry-Perot cavity at any time is given by the fields already present inside the cavity [1], the input field and the output field. The magnitude of the fields and the corresponding phase evolution of the fields can best be solved by discretizing the time in units of the round trip time $2T$, where T is the time it takes for the

---

[1] When referring to the field, the electrical field E is meant

field to travel the length L of the cavity.

To find the equations for all the relevant fields, we consider the situation as depicted in Fig. 7.2. The incoming field E_{in} is partially transmitted through mirror 1 and added to the already existing field to form the intracavity field E. The transmitted field is then a fraction of this intracavity field E, while the reflected field consists of two components, the promptly reflected field E_p and the leakage field from the cavity E_L. Finally, the cavity length can vary due to the displacements of mirrors 1 and 2. The distance between the two mirrors is defined using the length of the cavity and the displacement of both mirrors:

$$d(t) = L + X_2(t-T) - X_1(t) = L + \chi(t) \tag{7.1}$$

where we have taken into account the time delay of the field for traveling a distance L. Note that this time delay is negligible for short cavities, while for long cavities, such as LIGO, this time delay is significant.

With these ingredients, equations for the reflected and transmitted fields as well as the fields at mirrors 1 and 2 can be derived. The field inside the cavity at mirror 1 is given by[2]

$$E_1(t) = t_1 E_{in}(t) + r_1 r_2 \exp[-2ikd(t)] E(t-2T) \tag{7.2}$$

with t_1 the transmission coefficient of the first mirror, $r_1(r_2)$ the reflection coefficient of mirror 1 (2) and k the wave-vector, $\frac{2\pi}{\lambda}$, with λ the wavelength. The field at mirror 2 can now be expressed as follows:

$$E_2(t) = \exp[-ikd(t)] E_1(t-T). \tag{7.3}$$

The transmitted and reflected fields can be expressed similarly. This does require a reference plane to define the phase of the propagating field. Suppose the reference plane of the transmitted field is located a distance x after mirror 2. Similarly, the reference plane for the reflected field is located a distance x in front of mirror 1. It is now convenient to choose this distance x such that the phase factor $\exp(ikx)$ for traveling to the reference plane is 1. If this is assumed, the transmitted and reflected fields are the following:

$$E_{trans}(t) = t_2 \exp[-ikd(t)] E_1(t-T) \tag{7.4}$$

and

$$E_{refl} = \exp[-2ikX_1(t)] \left[r_1 E_{in}(t) - t_1 r_2 \exp[-2ikd(t)] E_1(t-2T) \right]. \tag{7.5}$$

Note that the component of the promptly reflected field, the first term in Eq. (7.5), has a positive sign, because the reflection occurs within the substrate of the mirror. Finally the input field $E_{in}(t)$ itself can have a certain phase ϕ. To account for this, the input field can be written as

$$E_{in}(t) = A \exp(i\phi) = A \exp(i\omega_L t) \tag{7.6}$$

with ω_L the laser frequency.

---

[2] Via the reflection coefficients r_1 en r_2 we account for the field leaving the cavity via mirror 1 and mirror 2.

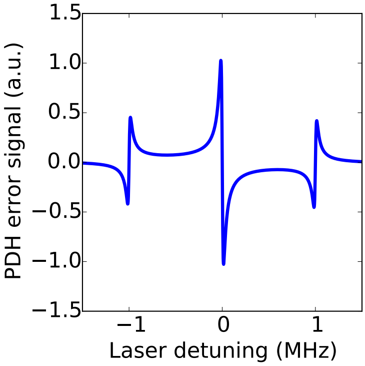

Figure 7.3: PDH error signal generated with the sum-over-round trips method.

Equations (7.1)-(7.5) have a recursive relationship between them, making them numerically solvable. To aid the computation, the cavity length and input laser frequency are chosen such that the phase factor $\exp[-ikd(t)]$ reduces to $\exp[-ik\chi(t)]$. In other words, we choose a frame rotating with the unperturbed cavity resonance frequency ω_{cav}. In this way, the earlier introduced laser frequency ω_L is relative to this unperturbed cavity resonance frequency.

Although the recursive Eqs.(7.1)-(7.5) can be solved for each consecutive round trip, this is not practical for short cavities. For example, for a 5 cm cavity, the round trip time is about 0.32 ns. If no processes occur on these timescales, lumping several round trips together will not significantly alter the end result. As we will see later, for our optomechanical setup the fasted process is the motion of the mechanical resonator, typically on the μs time scale, which makes this approximation justified.

Example: generating a Pound-Drever-Hall error signal

As an example, we can generate a PDH error signal and use this signal to detect the motion of one of the mirrors. The PDH method relies on a phase modulated beam reflecting off the cavity which is subsequently detected, demodulated and low-pass filtered (for details see Ref. [38]). From Eq. (7.6) it is clear that phase modulation of the input field is easy, by choosing ϕ as the following, $\phi = A_0 \cos \omega_M t + \omega_L t$, where we have introduced a modulation frequency ω_M and modulation depth A_0. By varying the laser detuning ω_L, the typical PDH error signal can be retrieved, as is shown in Fig. 7.3. This error signal is generated for a cavity with a linewidth of 28 kHz, a modulation frequency of 1 MHz and a time-step of $416 \times 2T$ to speed up the calculation.

Now that the PDH method is verified, we can make the end mirror oscillate and detect this motion. A periodic oscillation with an amplitude of 3 pm and a frequency of 75 kHz is applied to the end mirror. Fig. 7.4 shows the results of the PDH error signal as well as an FFT of the same error signal. The small oscillations visible in the PDH error signal are due to the remaining 2 MHz component, twice the modulation frequency, still present after filtering.

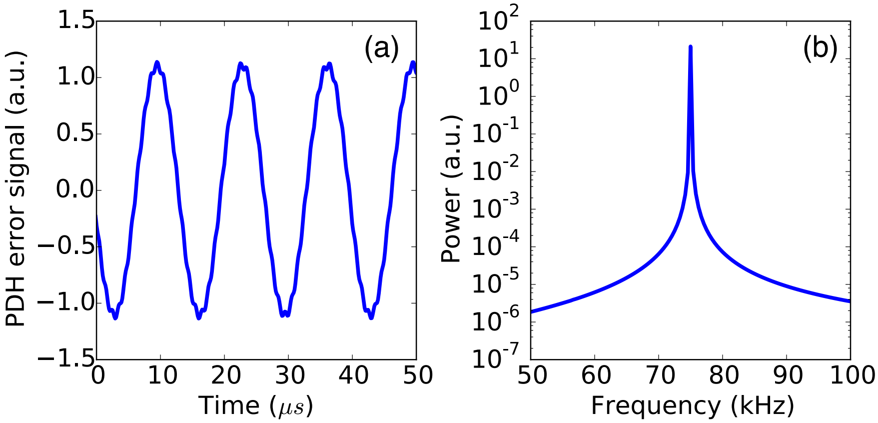

Figure 7.4: Detection of small mirror oscillations via the PDH method. (a) PDH error signal as function of time. (b) FFT of the error signal.

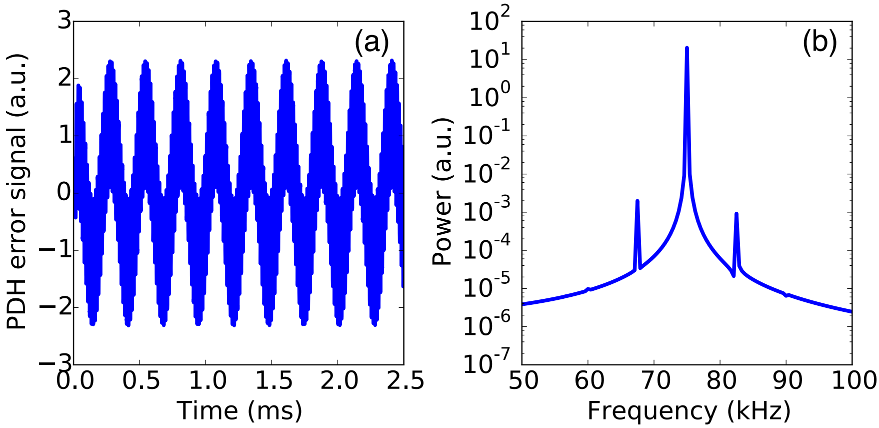

Figure 7.5: Detection of small mirror oscillations via PDH method. Compared to Fig. 7.4 a second component at 3.75 kHz is added. (a) PDH error signal as function of time. (b) FFT of the error signal.

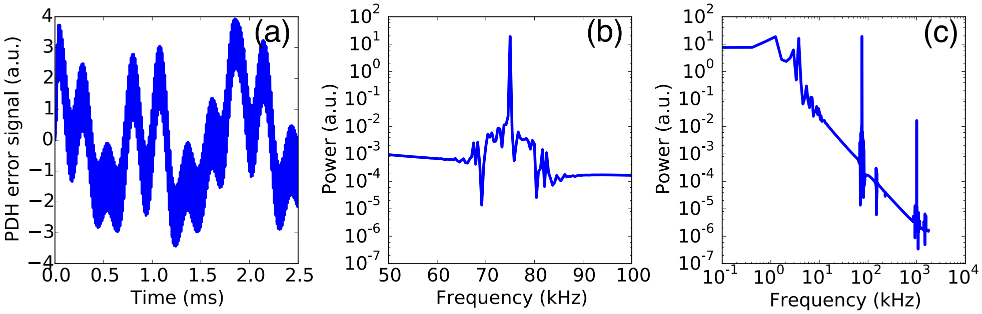

Figure 7.6: The effect of multiple unwanted oscillations in cavity length on the read-out of a movable mirror. (a) PDH error signal as function of time. (b) FFT of the error signal around the simulated mechanical resonance. (c) Same as (b) but showing the entire frequency scale.

Finally, the effect of mechanical vibrations can be simulated by adding an additional oscillation of the cavity length, in this case a displacement of 500 fm at a frequency of 3.75 kHz. The results are shown in Fig. 7.5. Although a low frequency oscillation is added, it also shows up as sidebands of the 75 kHz resonance in the FFT. Since a moving mirror in a cavity applies a phase modulation to the cavity field, for all frequency components present, the frequency component of 75 kHz in the optical field will have a 3.75 kHz modulation, resulting in the two sidebands.

When more low frequency components are present, this is no longer clear. In Fig. 7.6 three more unwanted oscillations of similar magnitude and frequency are added. Compared to Fig. 7.5 the noise floor has risen drastically due to the tails of the low frequency oscillations as can be seen in Fig. 7.6(c). Furthermore, a noise band around the frequency of interest starts to appear, making the individual sidebands no longer distinguishable.

7.2.3 Combining with optomechanical interaction

Until now only the read-out of a forced driven oscillation is considered, while in an optomechanical set-up the motion of the mirror is generated via thermal excitation and, depending on the laser detuning, the interaction with the cavity field. This interaction might be influenced when additional phase modulation of the cavity field occurs. To investigate this effect, the interaction with the movable mirror is taken into account as well. The mirror can be modeled as a harmonic oscillator with an additional force due to the radiation pressure:

$$\frac{d^2x(t)}{dt^2} = -\Gamma_m \frac{dx(t)}{dt} - \Omega_m^2 x(t) + \frac{2}{\pi m c} |E_2(t)|^2 + \eta(t) \tag{7.7}$$

with $x(t)$ the position of the mirror, Γ_m the mechanical damping rate in rad/s, Ω_m the mechanical frequency in rad/s, m the mass of the resonator in kg, c the speed of light and $\eta(t)$ the noise term that generates the mirror's thermal state, with $\left\langle \eta_i(t)\eta_j(t^{'}) \right\rangle = \frac{2}{m}\Gamma_m k_b T \delta_{i,j} \delta(t-t^{'})$.

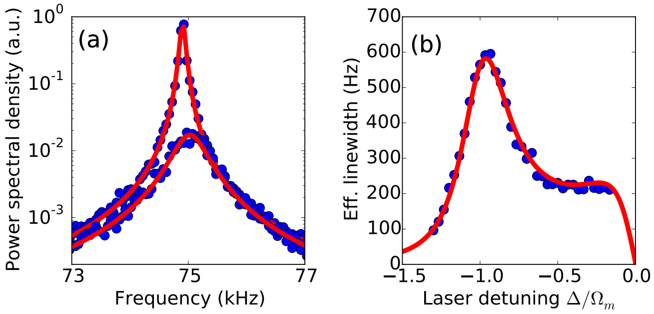

Figure 7.7: Full simulation of the optomechanical interaction. (a) Power spectra recorded via the PDH method for two different detunings. Red line is Lorentzian fit to extract the effective linewidth and center frequency. (b) and (c) show the effective linewidth and frequency shift for different laser detunings. The red lines is the expected trend from theory, based on the input parameters of the simulation.

To solve Eq. (7.7) together with the solution for the cavity field given by Eqs. (7.1) - (7.6), a modified 4th-5th order Runge-Kutta method is implemented. In this approach, the value of the cavity field and mirror position one time-step, h, further is calculated using approximated midpoint solutions and weighting them appropriately. For the approximate solution of $x(t)$ we can compute the resulting cavity field $E_2(t)$ and use this to calculate the effect on the mirror in the next approximated solution. After one round of calculations, when the next point of $x(t)$ is known, the final cavity field $E_2(t)$ is calculated.

To demonstrate the validity of this approach, we can simulate the read-out of the mirror motion with a weak probe laser via the PDH method introduced in the previous section, while the laser detuning of a second laser is varied. This model describes the experiment performed in chapter 5. The effect of the probe laser on the mirror is neglected for now, since the power of the probe laser is weak (50 nW compared to 1.3 μW for the cooling laser) and the probe laser is set at zero detuning, where the net optomechanical interaction is zero. Fig. 7.7 shows the result for a system at 300K with a mechanical frequency of 75 kHz, a mechanical Q-factor of $1{\times}10^5$ and an optical linewidth of 28.8 kHz. In Fig. 7.7(a) two power spectra are shown for different detunings, together with a Lorentzian fit. From this fit critical parameters such as effective linewidth and resonator frequency are extracted. Fig. 7.7(b) and 7.7(c) show the effective linewidth and resonator frequency shift for different laser detunings. The red line is the theory based on the input parameters of the simulation. An excellent agreement between simulation and theory validates our approach. Furthermore, the agreement between theory and simulation justifies the assumptions and simplifications made, such as the combination of multiple round trips into a single step.

We can now repeat the investigation of low frequency cavity vibrations on the read-out of the mechanical resonator. For this we introduce four low frequency cavity length oscillations, precisely the same as in Fig. 7.6, to generate vibrations in the

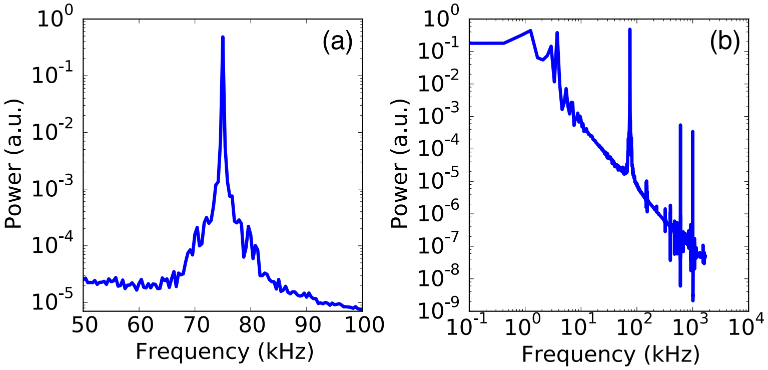

Figure 7.8: The effect of low frequency vibrations on the read-out of a moving mirror in an optomechanical system. (a) Power spectrum of simulated mechanical resonance. (b) Power spectrum showing the entire window.

cavity field. Figure 7.8(a) shows the mechanical resonance at 75 kHz, accompanied by additional features. Clearly the mechanical power spectrum can no longer be described by a Lorentzian. Figure 7.8(b) shows that the vibrations are also present in the low frequency part of the FFT of the PDH error signal. As with Fig. 7.6, the presence of the low frequency vibrations will also raise the noise floor in region of the mechanical resonance of interest.

7.2.4 Comparison with experiment

Fig. 7.8 shows that low frequency vibrations, via upconversion, can definitely cause the features visible in Fig. 7.1. However, any change in cavity length can be compensated for by adjusting the laser frequency to maintain the resonance condition:

$$\frac{\omega_L}{\omega_{cav}} = -\frac{\chi(t)}{L}. \tag{7.8}$$

Even partial compensation via the laser frequency should reduce the effect of low frequency vibrations, which in turn should change the vibrations visible around the mechanical resonance. In practice however, varying the PID settings of the laser lock does not change the observed mechanical displacement spectrum at all. Therefore low frequency vibrations are ruled out as the origin of the additional peaks seen in Fig 7.1. The important thing to remember, however, is that the system is extremely sensitive to low frequency lengths changes.

7.2.5 High-Q metals at low temperatures

Varying of the PID settings did not change the observed mechanical displacement spectrum, suggesting that low frequency vibrations are currently not an issue. Looking ahead, the entire optical set-up will operate at cryogenic temperatures inside a

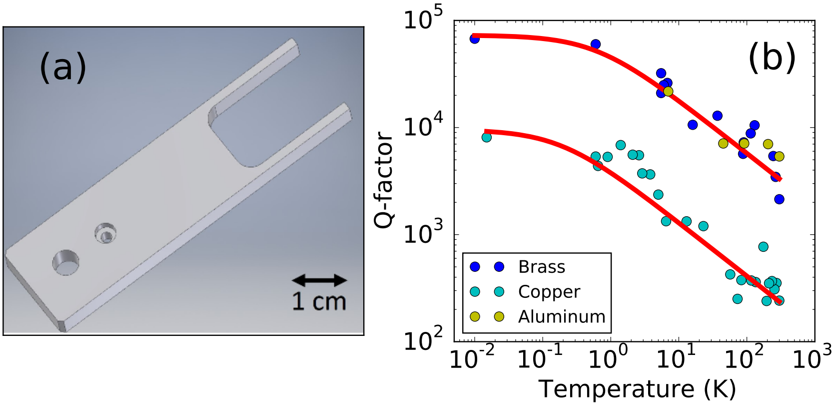

Figure 7.9: (a) Design of the metal tuning fork. (b) Q-factor as function of temperature for different metal tuning forks. The red line shows a fit of $Q \sim 1/\sqrt{T}$

cryostat cooled by a pulse tube cryocooler. Such cryocoolers are a source of low frequency vibrations which can easily excite mechanical modes of the optical set-up itself. Furthermore, at low temperatures the Q-factor of these mechanical modes can be drastically higher than at room temperature, leading to a larger amplitude of the mechanical modes.

To get a feel for this increase in Q-factor, several metal tuning forks are made with a frequency around 2 kHz, see Fig. 7.9(a). The Q-factor is obtained by driving the fundamental mode of the tuning fork with a piezoelectric element attached to the tuning fork and monitoring its motion via a fiber interferometer [100]. Alternatively, a mechanical ringdown is performed when the Q-factor is high (above 10000). Different metal tuning forks are mounted on the mixing chamber of a dilution refrigerator to measure the Q-factor as function of temperature. The results are shown in Fig. 7.9(b), together with a fit using $Q \sim 1/\sqrt{T}$.

Not surprisingly does the Q-factor increases when the temperature is lowered. What is interesting is that all three tuning forks seem to follow the same trend: $Q \sim 1/\sqrt{T}$. The only tentative explanation we have so far for this relation is the following: the displacement of a harmonic oscillator, such as lattice vibrations in metals, scales with $\sqrt{T}$. If the mechanical dissipation in metals depend on the amplitude of the lattice vibrations, this would explain the relationship $Q \sim 1/\sqrt{T}$. Of course, this hypothesis does require more measurements.

On a more practical note: the Q-factor of the brass tuning fork increased from 5000 at room temperature to 75000 at cryogenic temperatures. This suggests it is not unlikely that when the optical set-up, made of brass, functions perfectly at room temperature, at low temperatures vibrations can become an issue. Therefore, performing measurements at low temperatures does require a cryogenic compatible vibration isolation preferably together with a low-Q set-up. In chapter 10 we will discuss the vibration isolation in more detail.

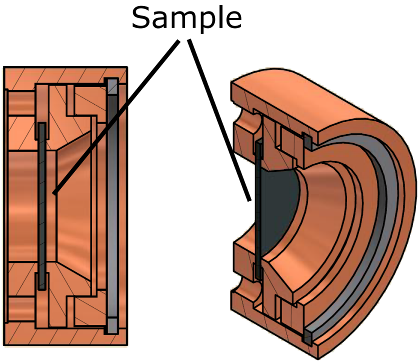

Figure 7.10: The sample holder. The sample, a silicon chip, is clamped down by two gold coated copper rings held in place by a wave spring washer.

7.3 Noise from sample

Another candidate for the mechanical vibration peaks visible in Fig. 7.1 are modes of the sample itself. Sixteen trampoline resonators reside on a single silicon chip approximately 15 × 15 mm. The chip itself is clamped down by two gold coated copper rings held in place by a wave spring washer, see Fig. 7.10. A back-of-the-envelope calculation shows that a clamped silicon wafer of this size has modes between 100 and 500 kHz [101]. Because the wafer also contains square holes with trampoline resonators, the number of modes can become more complex. It is therefore likely we should pick-up some of these modes.

As a first step to investigate this, a single sample was remounted several times leading to a change in resonance frequency, as well as mechanical quality factor (Q-factor). This already is a good indicator that the clamping of the wafer is an issue. However, the mechanical spectrum remains noisy. As a next step, the method of clamping was varied. The clamping force was increased and one copper rings was interchanged for a ring made of Vespel. Again, changes in resonance frequency and Q-factor were observed, but no reduction in the number of peaks.

To potentially reduce the number of modes present on the wafer, single trampoline resonators on a chip were fabricated. Because silicon nitride with a lower stress was used, the mechanical frequency was reduced from ~ 300 kHz to around ~ 80 kHz. Both the change in geometry and frequency did not resolve the issue of the additional mechanical peaks.

The wafers used to fabricate the samples are super polished silicon wafers. Therefore, the surface is truly flat. The rings used to clamp down the sample can never be made flat with the same precision. To ensure a good contact between the rings and sample, two sheets of indium foil, 30 μm thick, were placed on either side of the sample. When clamping down the sample, the indium will yield, ensuring a good mechanical contact. The resulting mechanical power spectra are shown in Fig. 7.11.

In the left panel of Fig. 7.11 the mechanical power spectra are shown for the sam-

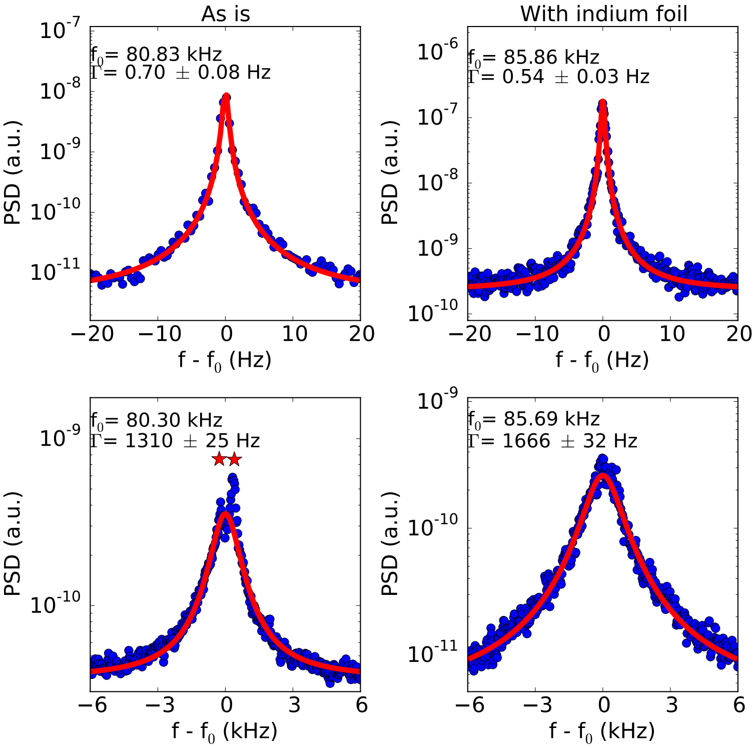

Figure 7.11: Mechanical power spectra of the same sample before and after clamping down using indium foil. The bottom panels compares the two cases with strong optical cooling. The sample without indium shows two additional peaks indicated with red stars.

ple clamped without indium. The bottom left panel shows the Lorentzian resonance and two additional mechanical peaks, when a strong cooling beam is present. If the same sample is clamped down between indium foil, several things happen. Not only has the resonance frequency increased significantly, but also the Q-factor has increased.[3] Furthermore, when now a strong cooling beam is applied, the spectrum remains completely clean, as can be seen in the bottom right panel of Fig. 7.11.

Indium is of course not the best choice to use, because it becomes superconducting below 3.4 K resulting in poor thermal conductivity. Also, the process of placing the indium is prone to errors. A better alternative would be to isolate the trampoline resonator from the remaining part of the chip. One way would be to place a phononic bandgap shield around the resonator [102, 103]. For our type of resonators, with a frequency between 100 - 300 kHz, this leads to a significantly larger chip size and is therefore not ideal. Instead, we have chosen to surround the resonator with a second, larger trampoline resonator. This outer resonator with a frequency of 2 - 4 kHz, acts as a mechanical low-pass filter.

We have demonstrated (see Weaver et al. [35]) that such a system provides at least 60 dB of isolation. But more importantly, the mechanical properties are now independent of the method of mounting. In the next chapter we will show that the mechanical power spectrum is clean, consisting only of the Lorentzian resonance of interest.

---

[3] Remember: $Q = f_0/\Gamma$